

<https://doi.org/10.1038/s42005-024-01594-w>

Laboratory evidence of confinement and acceleration of wide-angle flows by toroidal magnetic fields

Check for updates

Z. Lei^{1,2,11}, L. X. Li^{1,11}, Z. H. Zhao¹, W. Sun³, H. H. An⁴, D. W. Yuan⁵, Y. Xie¹, W. Q. Yuan¹, S. K. He⁶, L. Cheng⁷, Z. Zhang⁷, J. Y. Zhong³, W. Wang⁴, B. Q. Zhu⁸, W. M. Zhou⁶, C. T. Zhou⁹, S. P. Zhu², J. Q. Zhu⁸, X. T. He² & B. Qiao^{1,10} ✉

Astrophysical jets play crucial roles in star formation and transporting angular momentum away from accretion discs, however, their collimation mechanism is still a subject of much debate due to the limitations of astronomical observational techniques and facilities. Here, a quasi-static toroidal magnetic field is generated through the interaction between lasers and a four-post nickel target, and our all-optical laboratory experiments reveal that a wide-angle plasma plume can be collimated in the presence of toroidal magnetic fields. Besides the confinement effects, the experiments show the jet can also be accelerated by the enhanced thermal pressure due to the toroidal magnetic fields compressing the flow. These findings are verified by radiation magneto-hydrodynamic simulations. The experimental results suggest certain astrophysical narrow plasma flows may be produced by the confinement of wide-angle winds through toroidal fields.

Astrophysical jets, representing supersonic highly-collimated plasma beams, are observed to emerge in numerous astronomical objects, from young stellar objects (YSOs) to active galactic nucleus (AGNs). While AGN and/or extragalactic jets are mostly relativistic and connected with the production of high-energy cosmic rays^{1,2}, YSO jets also called Herbig-Haro (HH) objects³ have recently aroused much interest as they play a crucial role in redistributing mass, energy and angular momentum between the dense core and parent cloud during the formation of stars^{4,5}. However, due to the limitations of astronomical observational techniques and the complex astrophysical environment, the physical mechanisms of jet eruption, collimation, and acceleration are still unclear so far. For example, although the new data obtained from the Hubble Space Telescope (HST) reveals that it is possible to track the collimated jet down to a distance of 20 AU from the source⁶, a number of studies suggest that the primary process of collimation takes place at the scales 10 AU^{4,7,8}, and various emissions from the jet source

and its surrounding complex background cloud bring further difficulties to direct observations. After decades of investigations from numerical simulations^{9,10}, and observational data^{11,12}, it is believed that the presence of a magnetic field plays a key role in YSO jet dynamics¹³. Furthermore, a significant number of astronomical observations^{11,14,15} have directly and/or indirectly verified the existence of both the poloidal and toroidal magnetic fields around HH objects.

The collimation and feedback of YSO jets in the presence of magnetic fields with various topologies and under different spatiotemporal scales have been widely investigated^{16–18}. The magneto-centrifugal model¹⁹ is one of the most widely accepted concepts of magnetized disk winds. A large-scale poloidal (axial) magnetic field is assumed to be anchored in a Keplerian accretion disk. In the surrounding space close to the disk surface where the magnetic energy density is much larger than the plasma thermal and kinetic energy densities, i.e., the ratio of plasma to magnetic pressures $\beta < 1$, the

¹Center for Applied Physics and Technology, HEDPS, and State Key Laboratory of Nuclear Physics and Technology, School of Physics, Peking University, Beijing 100871, People's Republic of China. ²Institute of Applied Physics and Computational Mathematics, Beijing 100094, People's Republic of China. ³Department of Astronomy, Beijing Normal University, Beijing 100875, People's Republic of China. ⁴Shanghai Institute of Laser Plasma, CAEP, Shanghai 201800, People's Republic of China. ⁵Key Laboratory of Optical Astronomy, National Astronomical Observatories, Chinese Academy of Sciences, Beijing 100012, People's Republic of China. ⁶Science and Technology on Plasma Physics Laboratory, Laser Fusion Research Center, China Academy of Engineering Physics, Mianyang 621900, People's Republic of China. ⁷Beijing National Laboratory for Condensed Matter Physics, Institute of Physics, Chinese Academy of Sciences, Beijing 100190, People's Republic of China. ⁸National Laboratory on High Power Laser and Physics, Chinese Academy of Sciences, Shanghai 201800, People's Republic of China. ⁹Center for Advanced Material Diagnostic Technology, Shenzhen Technology University, Shenzhen 518118, People's Republic of China. ¹⁰Frontiers Science Center for Nano-optoelectronic, Peking University, Beijing 100094, China. ¹¹These authors contributed equally: Z. Lei, L. X. Li. ✉e-mail: bqiao@pku.edu.cn

plasma is tied to and free to move along the poloidal magnetic field lines, since the Lorentz force only has perpendicular components. Along the field line, the centrifugal force increases with distance from the axis. When the component of the centrifugal force along the field line exceeds that of gravity, the plasma tied to the field line is accelerated outward, launching a plasma outflow. This centrifugal process stops at the Alfvén surface when the outflow velocity becomes comparable to the Alfvén speed because the field is no longer strong enough to enforce corotation. Beyond the Alfvén surface, the magnetic field energy density becomes smaller than the plasma thermal and kinetic energy densities²⁰, that is $\beta > 1$. As a result, the inertia of the plasma causes it to lag behind the rotation of the field line, and the magnetic field gets spiraled, eventually resulting in the formation and gradual domination of the toroidal magnetic field component. The presence of a large-scale toroidal magnetic field provides hoop stress leading to self-confinement, effectively addressing the problem of jet collimation²¹, and potential further magnetic acceleration²².

Laboratory experiments^{23–25} have demonstrated that stable and narrow collimation of laser-produced plasma flow can result from the presence of a uniform poloidal magnetic field, which is used to mimic the role of the poloidal magnetic field on the formation of astrophysical jets⁹. The poloidal magnetic field is a crucial factor in the collimation of astrophysical jets. Previous studies^{23,26} have demonstrated that the poloidal fields are capable of confining a wide-angle plasma outflow, resulting in the formation of a sizable cavity. Consequently, a collimated jet emerges from the plasma nozzle. However, experiments on the spheromaks²⁷ and Z-pinch²⁸ facilities have shown that propagations of plasma flows are disrupted with several knotty structures formed due to the kink instabilities^{29–31} occurring in the presence of toroidal magnetic fields, where the reason that leads to the contradiction is that there $\beta < 1$. Recent experiments on the pulsed-power facilities³² have shown a collimated jet can be formed within the toroidal magnetic fields when the plasma $\beta \sim 1$, or a little higher than unity. The length-to-width ratio of the obtained jet is rather small, and hard to compare with the astronomical observations. To further increase plasma β on these pulsed-power facilities may be extremely difficult since the plasma itself is driven by external electric currents. Magnetic fields also play a significant role in the field of inertial confinement fusion (ICF)³³. Magnetic fields can effectively reduce electron heat conduction³³ and have a certain inhibitory effect on small-scale Rayleigh-Taylor instabilities³⁴. Researchers discovered that the closed toroidal magnetic field lines can significantly enhance temperature. However, specific methods to generate the toroidal topology in laser-driven experiments are still lacking in experimental setups³⁵.

Here we report on results of the all-optical scaled laboratory experiments, where both the large-scale toroidal magnetic fields and wide-angle expanding plasma outflows are driven by high-power lasers, creating extreme conditions representative of those of YSO jets. In the experiments, the strong toroidal magnetic field is generated from an innovative open-ended four-post nickel (Ni) target driven by ns lasers, whose topology and strength are verified by both proton radiography and B-dot probe. The plasma outflow is driven from the rear side of a polyethylene (CH) foil target, which initially undergoes nearly isotropic expansion. The Nomarski interferometer images clearly show that a narrow, directional jet can be formed from the confinement of the isotropically expanded plasma flow in the presence of toroidal magnetic fields. Besides the confinement effect, we find that the jet also undergoes acceleration by the enhanced thermal pressure due to confinement of the toroidal magnetic fields, when it transports from strong to weak field regions, inversely to the field strength gradient direction. Otherwise, the opposite. The experimental results are reproduced by two-dimensional (2D) and three-dimensional (3D) radiation magneto-hydrodynamic (RMHD) simulations. Further, similar scaling laws show that our experimental results can be applied to suggest the astrophysical narrow plasma flow can be produced by the confinement of wide-angle winds through toroidal fields. Note that collimation of wide-angle outflow may be a multi-physical coupling behavior, our findings do not preclude the radiation-cooling effect³⁶ and the inertial collimation effect by the ambient media³⁷.

Results

Experimental setup

The experiments are carried out at ShenGuang-II (SG-II) laser facility in China with the setup shown schematically in Fig. 1. As shown in Fig. 1a, the supersonic plasma outflow is driven by four nanoseconds (ns) laser pulses from the rear side of the CH target [Fig. 1d], which consists of a 1.5-mm-diameter, 10- μ m-thick CH foil, in contact with a CH “washer” with a central, cylindrical hole of 300- μ m diameter. The lasers heat and blow out the foil, creating a flow of heated CH plasmas down the cylindrical hole in the washer and eventually out of the hole forming the supersonic plasma outflow³⁸. The CH material used here precludes the radiation-cooling effect. According to the estimated temperature in the previous research³⁹, the CH plasma is well-ionized. The large-scale strong toroidal magnetic fields are generated by interactions of the other four ns lasers with the open-ended four-post Ni target that is composed of four posts connected with a planar plate. As shown in Supplementary Fig. S1, Fig. S2, and Fig. S3 and the corresponding detailed explanations (see Supplementary Note 1), due to the escaping of a large number of energetic electrons⁴⁰, a large electrical potential develops between the posts and planar plate when lasers irradiate the latter, which drives the cold electron currents in four posts so that a toroidal magnetic field topology is formed, shown by the toroidal lines in Fig. 1a. The strength of such a toroidal magnetic field drops with the distance away from the Ni posts, therefore in the case of Fig. 1a, the plasma outflow moves inversely to the gradient of the toroidal magnetic field from strong to weak regions, while in the case of Fig. 1f, it moves along the field strength gradient (we call as “the comparative case” hereinafter). Both CH and Ni targets are mounted to a Cu target holder in experiments. Note that the 10- μ m thickness of CH foil is chosen based on RMHD simulation results to ensure the plasma outflow transport during the living time of the magnetic field because the maximum time delay between different laser pulses on the SG-II facility is limited.

The main diagnostics are the X-ray pinhole camera, B-dot probe, and optical diagnostics (Nomarski interferometer and shadowgraphy), whose details are shown in Supplementary Figs. S4 and S5 (see Supplementary Note 2). As seen in schematic Fig. 1b, the probe laser is transmitted along the x -axis, and the B-dot probe is placed in $(X, Y, Z) = (-44, 0, 12)$ in units of mm, 46mm away from the center, where the zero position of the axes is placed at the center of CH foil. The time delays of different ns laser pulses as well as the probe laser are shown in Fig. 1c, labeled respectively as T_0 , T_1 , and T_{probe} . The side-on views of three types of targets used in experiments are shown in Fig. 1d–f, with detailed parameters labeled.

Laser-driven toroidal magnetic field

To verify the toroidal magnetic field generation, we perform the experimental shot by laser irradiation of the Ni target only, where the CH target is unmounted. The Nomarski interferometer images are analyzed by the inversion program so that clear fringe images are obtained. More details of the inversion program for the interferometry image data are given in Supplementary, see Fig. S6 (in Supplementary Note 3). The corresponding fringe images at the top of the Ni posts are shown in Fig. 2a, b, respectively without and with laser irradiations. We see there is almost no movement of the fringes in the z -axis direction after even 3 ns from laser irradiation, which implies that the expansion of the Ni plasmas in the z -axis can be neglected, precluding their effects on jet collimation. The original data of the B-dot probe as well as the corresponding integrated B-field signal are shown in Fig. 2c, d. They show the magnetic field strength at the place of the B-dot probe is about a few mT with a duration of about a few ns, and the peak strength is 3.8 mT.

To get the spatial distribution of the magnetic field, the magnetostatic code “Radia”⁴¹ is used, where the electric currents within the Ni posts are adjusted to match the B-field strength measured at the B-dot position, as shown in Fig. 2f. The current within each Ni post is set at about $I = 16$ kA, and the total current is about $I = 64$ kA. Fig. 2g plots the obtained 3D spatial distributions of the magnetic field, where similarly the zero point is set on the center of CH foil [Fig. 2e]. We see from Fig. 2g that the magnetic field does show a toroidal topology above the four-post target, and it is axisymmetric.

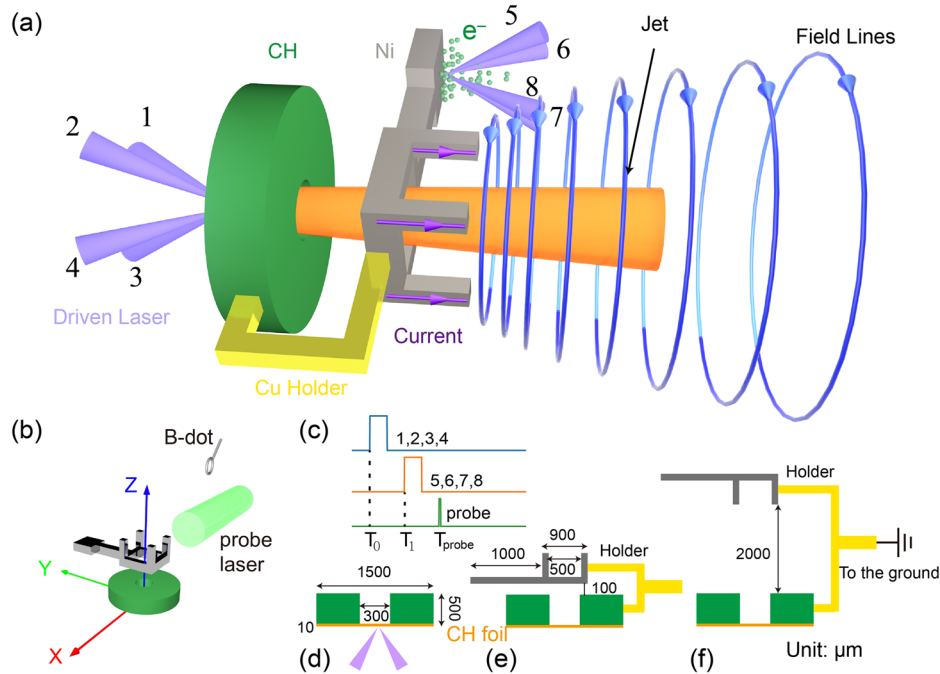


Fig. 1 | Schematic view of the experimental setup. **a** Plasma outflow and toroidal magnetic field generation: the supersonic plasma outflow is driven by four (“1”–“4”) nanosecond-laser pulses from the rear side of the polyethylene (CH) foil target (orange); the toroidal magnetic fields are generated by interactions of the other four (“5”–“8”) nanosecond-laser pulses with the nickel (Ni) target (gray) that are composed of open-ended four posts connected with a planar plate; both the CH and Ni targets are mounted on a copper (Cu) holder (yellow). In this case, the plasma outflow moves inversely to the gradient of the toroidal magnetic field strength from strong to weak regions. **b** Schematic view of the experimental diagnostics: the B-dot probe and optical Nomarski interferometer diagnostics. The axes defined in the experiment are also shown here, where the zero position on the z-axis is the position of CH foil. **c** Time delays of different laser pulses (“1”–“8”) as well that of the probe

laser for the optical Nomarski interferometer diagnostics, labeled respectively as T_0 , T_1 and T_{probe} (The variable T_0 denotes the moment when the driven laser initiates interaction with the CH target; T_1 signifies the onset of interaction between the driven laser and the Ni target; and T_{probe} indicates the trigger time of the probe laser.). **d–f** are the side-on schematic views for three types of targets used in experiments with their detailed parameters labeled. Panel **d** corresponds to the target in the free-expansion case, consisting of a 1.5-mm-diameter, 10- μm -thick CH foil, in contact with a 500- μm -thick CH “washer” with a central, cylindrical hole of 300- μm -diameter. **e** corresponds to that in panel **a**. **f** corresponds to the target in the comparative case where the plasma outflow moves along the gradient of the magnetic field from weak to strong regions.

The magnetic field lines near the posts show a four-leaf clover-like structure [see the red lines], where its strength has a maximum value of about 20 T and drops rapidly with the distance. The 2D slices of the magnetic fields in the yz-plane and xz-plane are shown in Fig. 2h, i, respectively.

To double-check the magnetic field topology and strength, additional proton radiography experiments are carried out on SG-II Upgrade laser facility, where we use energetic protons driven by petawatt ps laser to probe the magnetic field from the face-on direction. Details of the experimental setup are described in the supplementary Fig. S7 (see Supplementary Note 4). The radiography image at $t = 1.3\text{ns}$ in Fig. 2j shows that protons are deflected to the outside region of four Ni posts and a ring structure is formed (see the red dotted line), clearly implying that the field topology is indeed toroidal. According to the paraxial approximation⁴², the path-integrated magnetic field Ψ can be obtained as $\Psi \approx 1.31 \times 10^4 \text{Gs} \cdot \text{cm}$ [see section “Proton Radiography Experiment” in the supplementary]. Assuming the length of the magnetic field in z-axis equals the length of Ni posts (about 600 μm), the magnetic field strength is estimated as $B \approx 21.8\text{T}$, in consistency with that shown in Fig. 2f. By using the inverse field-reconstruction program “PROBLEM”⁴³, we obtained the reconstructed path-integrated magnetic field Ψ , shown in Fig. 2k, further verifying its toroidal topology. To determine whether a proton photographic image is in a caustic state [see Fig. S8 and Supplementary Note 4 in the supplementary], we can refer to the definition provided in Equation 11 of previous work⁴⁴. By employing $\mu = h\alpha/a$ qualitatively, where h represents the distance from the proton source to the plasma, α denotes the proton deflection angle, and a represents the longitudinal characteristic scale of the magnetic field. Here $\mu = 0.33 < 1$, indicating that the proton photographic image is in a nonlinear injective regime. Consequently, the PROBLEM program can be applied to invert

Fig. 2j]. The corresponding synthetic numerical proton radiography image by using the magnetic fields [Fig. 2g] obtained from the Radia simulation is shown in Fig. 2l, agreeing well with the experimental results in Fig. 2j.

Free expansion of laser-driven plasma outflow

To show how laser-driven plasma outflow expands freely in a vacuum (in the absence of any magnetic fields), we carry out the experimental shot by laser irradiation of the CH target only, where the Ni target is unmounted, as shown in Fig. 1d. The original Nomarski interferometer images at delay times of respectively 3, 5, and 7 ns are shown in Fig. 3a–c. Note that, because of its low intensity (see Supplementary Fig. S4 and Supplementary Note 2), the probe laser here is almost fully absorbed and/or deflected by laser-driven plasma outflows, leading to the invisibility of the interference fringes inside the plasma outflows. However, we can still see the outlines of plasma outflows through the clear fringe edges in these images. At delay time $t = T_0 + 3\text{ns}$ [Fig. 3a], the CH plasma outflow moves just out of the cylindrical hole, having a full-width-at-half-maximum (FWHM) width of about 734 μm and length of about 1084 μm (measured from the initial position of CH foil). Afterward, the outflow undergoes rapid transverse expansion driven by the thermal pressure, resulting in an increase of the width by 2 times in only 2 ns up to 1525 μm [see Fig. 3b]. This wide-angle plasma outflow eventually reaches a 1:1 length-to-width ratio with a propagation velocity of about 250 km/s.

Both 2D and 3D RMHD simulation results in respectively Fig. 3d–f, g–i verify the rather similar physical processes as the experiments. It needs to be explained that there is a certain mismatch in the width of the outflow between the experimental and numerical simulation results. While, despite this mismatch, it is still possible to describe the overall dynamics evolution of

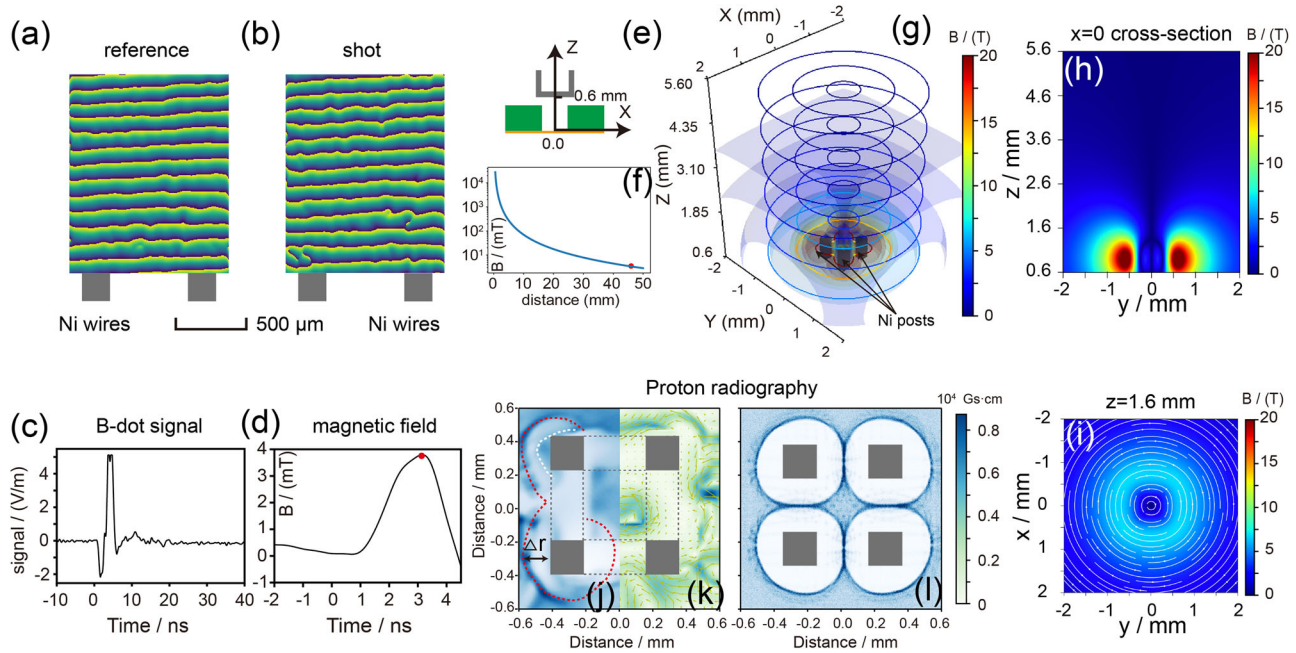


Fig. 2 | Results of toroidal magnetic field production in experiments. **a, b** The Nomarski interferometer fringe images (analyzed by the inversion program) for plasma densities around nickel (Ni) posts (wires) for the cases of respectively without and after 3 ns with laser irradiation. **c, d** The original data of the B-dot probe and the corresponding integrated magnetic field signal, whose acquisition bandwidth is 3 GHz. The peak magnetic field strength is about 3.8 mT (see the red dot). **e** The axis used to show the magnetic field, the zero point is placed at the center of the polyethylene (CH) foil. **f** The amplitude of the generated magnetic field varies with the distance from the open-ended four-post target $Z = 0$ to the B-dot probe position (the red dot at $Z = 46$ mm), which is used for adjusting the current setup in the “Radia” simulation. **g** 3D spatial distribution of the generated magnetic field calculated through the magnetostatic code “Radia”. The Ni posts are labeled by the gray cuboids

(pointed by the black arrows). The circle lines are the magnetic field lines and the colors on the lines represent the field strengths. The isosurface map of the magnetic field is also shown in **g**, and the field strengths of different surfaces are (1,2,4,8,10,15,20) T respectively. **h, i** Distributions of the toroidal magnetic fields in respectively the yz -plane [cut at $x = 0$] and xy -plane [cut at $z = 1.5$ mm], where the white lines represent the field lines. **j–l** are the results of proton radiography experiment, where **j** is the face-on radiography image at $t = 1.3$ ns (where t represents the time), **k** is the reconstructed path-integrated magnetic fields Ψ (in units of Gs · cm) through the inverse “PROBLEM” program, with field lines represented by the yellow arrows, and **l** is the corresponding synthetic numerical proton radiography images based on the magnetic fields in **g** obtained from the Radia simulation.

the outflow. The plasma number density at the edge of the outflow is about $6 \times 10^{18} \text{cm}^{-3}$, and the core number density within the cylindrical hole is up to $3 \times 10^{21} \text{cm}^{-3}$. The electron temperature at the central part of the plasma outflow is $30 \sim 40 \text{eV}$, and the corresponding sound speed (c_s) is about 65km/s . Therefore, we estimate that the plasma outflow is supersonic with the Mach number $M_a \approx 4$. In the simulations, the self-generated Biermann magnetic fields are also included [see the map plot with green colorbar in Fig. 3i], which is about a few T and only distributes at the plasma surface region, too weak to achieve self-collimation.

Laser-driven scaled plasma jet

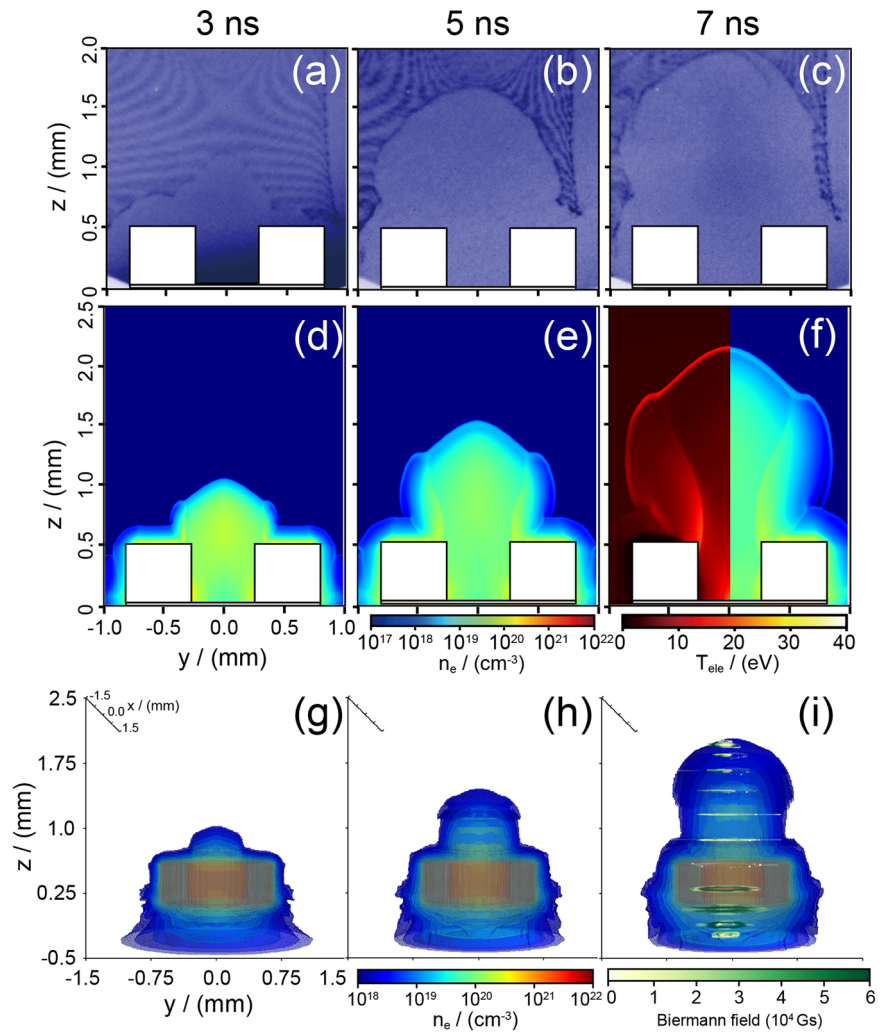
When both the CH and Ni targets are mounted, the scaled plasma jets are formed by confinement of the above laser-driven wide-angle plasma outflows in the presence of toroidal magnetic fields. For more consistent comparisons, we perform shots by two types: one-side shot where only the CH target is irradiated by “1”-“4” ns lasers [see Fig. 4c], and two-side shot where both the CH and Ni targets are irradiated with respectively “1”-“4” and “5”-“8” nanosecond lasers [see Fig. 4d], and the delay time between them is $T_1 = T_0 + 2\text{ns}$ [see Fig. 1c]. Fig. 4a plots the B-dot signals for respectively the free-expansion, one-side, and two-side shots, where the zero time is defined as the time when the signal fluctuates significantly. On the one hand, we see for both one-side and two-side shots the B-dot signal is much stronger than that of the free-expansion case. On the other hand, for the one-side shot, only one B-dot signal with a duration of a few ns is excited, which corresponds to the magnetic field driven by the cold electron current in the Ni posts due to the induced electric potential between CH and Ni targets (as they are both mounted on the Cu holder) when lasers irradiate on the CH target, while for the two-side shot, two signals are excited, where besides the same signal as that in the one-side shot, another much stronger

and longer signal appears, which corresponds to the toroidal magnetic field generated when the other four lasers irradiate the Ni target. After integration of the B-dot signal, we see from Fig. 4b that the toroidal magnetic field in the two-side shot case has larger strength (peak value at about 10 mT) and longer duration (about 20–30 ns) than that in the one-side shot case, and it is almost zero for the free-expansion case.

The plasma outflow density distributions at delay time $t = T_0 + 5\text{ns}$ can be seen from the original Nomarski interferometer images in Fig. 4e, g for, respectively, the one-side and two-side shots, where the higher-intensity ninth beam of the SG-II laser facility is used as the probe laser so that clear fringe shifts are observed. After the inversion by our inversion program, the corresponding plasma density distributions can be given, as shown in Fig. 4f, h, respectively. We see clearly that, compared with the free-expansion case [Fig. 3b], here for both one-side and two-side shots, the lateral expansion of plasma outflow is significantly suppressed by the z -axis perpendicular Lorentz force of the toroidal magnetic field, so that the wide-angle plasma outflow is collimated to form a narrow jet. For the one-side shot [Fig. 4e, f], a jet with a maximum density of about $6 \times 10^{19} \text{cm}^{-3}$, length-to-width ratio of 3:1 (length 2075 μm , width 680 μm) is obtained, where the jet velocity is also increased to 400 km/s. Furthermore, for the two-side shot, due to the presence of much stronger toroidal magnetic fields, we see from Fig. 4g, h that a much more narrow and stable jet with a maximum density up to $7 \times 10^{20} \text{cm}^{-3}$, length-to-width ratio of 8:1 (length 3009 μm , width 363 μm) is formed, where the jet is also accelerated to have a much higher velocity as 600 km/s.

The lengths and widths of the plasma outflows varying with time for different experimental shots are summarized in Fig. 4i, j, respectively. From the fitting of them for the free-expansion case (see the black lines), we estimate that the plasma outflow has a longitudinal transport velocity of

Fig. 3 | Experimental and radiation magneto-hydrodynamic (RMHD) simulation results for free expansion of laser-driven polyethylene (CH) plasma outflow. **a–c** The Nomarski interferometer images at delay times of 3, 5, and 7 ns after T_0 respectively (where T_0 represents the time at which the driven laser begins to interact with the CH target.), where the initial positions of the CH target are marked with the white cubes. **d–f** Plasma outflow density distributions at the corresponding times obtained from 2D RMHD simulations (under the cylindrical coordinates), where the left panel of **f** shows the electron temperature distribution. **g–i** Isosurface plots of plasma outflow densities from 3D RMHD simulations, where the lines with green colorbar show the self-generated Biermann magnetic field.



about 240 km/s and transverse expansion velocity of about 170 km/s, and from the density map after inversion of the Nomarski interferometer images, we estimate that the average ion number density around the plasma outflow is about $1\text{--}2 \times 10^{19} \text{g} \cdot \text{cm}^{-3}$, so the plasma beta is around $\beta \approx 10 \sim 50 \gg 1$ (the temperature is estimated as 80–100 eV, see Fig. 5f) at the edge of the plasma jet. Comparing the two-side shots with the free-expansion case, we further verify the confinement and acceleration effects of jets due to the toroidal magnetic field, where the formed jet has a longitudinal directional transport velocity of 602 km/s much larger than the transverse expansion velocity of 73 km/s.

Figure 4m, n show the corresponding Nomarski interferometer images for the comparative case of, respectively, one-side [see Fig. 4k] and two-side [Fig. 4l] shots, where the direction of the Ni target is adjusted and the separation distance between CH and Ni targets are increased so that the plasma outflow transports along the gradient of the generated toroidal magnetic field. By contrast, we see that the plasma jet undergoes deceleration during the collimation process because of the negative parallel component of the magnetic pressure. For the one-side shot, although the width of the plasma outflow is reduced to $564 \mu\text{m}$, its transport distance is decreased to $1532 \mu\text{m}$, even less than the free-expansion case. For the two-sided shot, the transport distance of the plasma outflow is further decreased to $1431 \mu\text{m}$. The top of the plasma jet shows an inverted-triangle-like structure [the red box in Fig. 4n].

RMHD simulations for jet confinement and acceleration

2D RMHD simulations are performed with the “FLASH” code⁴⁵ under the cylindrical coordinates, which has been developed to include many high-

energy density physics modeling capabilities including laser energy deposition, multi-temperature ($T_e \neq T_i \neq T_{\text{rad}}$), electron thermal conduction, radiation diffusion, etc. The detailed simulation setup and parameters are given in the Methods, which are all consistent with those in experiments. For self-consistency, we directly use the magnetic field obtained from the “Radia” simulation [shown in Fig. 2g] as the input for the RMHD simulation. Fig. 5a shows the distributions of the plasma density at time $t = T_0 + 5 \text{ns}$ obtained from the simulations for one-side cases in acceleration scenarios. The width of the plasma flow is about $700 \mu\text{m}$ [see Fig. 5a], and the wide-angle outflow has experienced a certain degree of confinement due to toroidal fields, as indicated by the streamlines. Fig. 5b plots the corresponding distributions of the toroidal magnetic fields and the corresponding Lorentz force. The magnetic field at the edge of the plasma flow is effectively compressed and amplified to the magnitude of 30 T. The Lorentz force is mainly horizontal inward, shown by the black arrow lines in the right parts of Fig. 5b, which suppresses the lateral expansion of plasma outflow, resulting in confinement of wide-angle outflow. For the two-side case in acceleration scenarios [see Fig. 5b], due to the presence of stronger magnetic fields, the lateral expansion of the outflow is significantly suppressed, resulting in the wide-angle outflow being well confined to a narrow flow. Fig. 5d shows the corresponding magnetic fields and the Lorentz forces, which both distribute only at the lateral edge regions of the plasma jet and decrease with the distance along the Z-direction. It can be observed that the magnetic field does not exhibit a significant compression amplification phenomenon as in the one-sided case. At the bottom of the plasma flow, the initial strong magnetic field is already sufficient to confine the lateral expansion of the outflow. On the other hand, as seen in Fig. 5e, because of

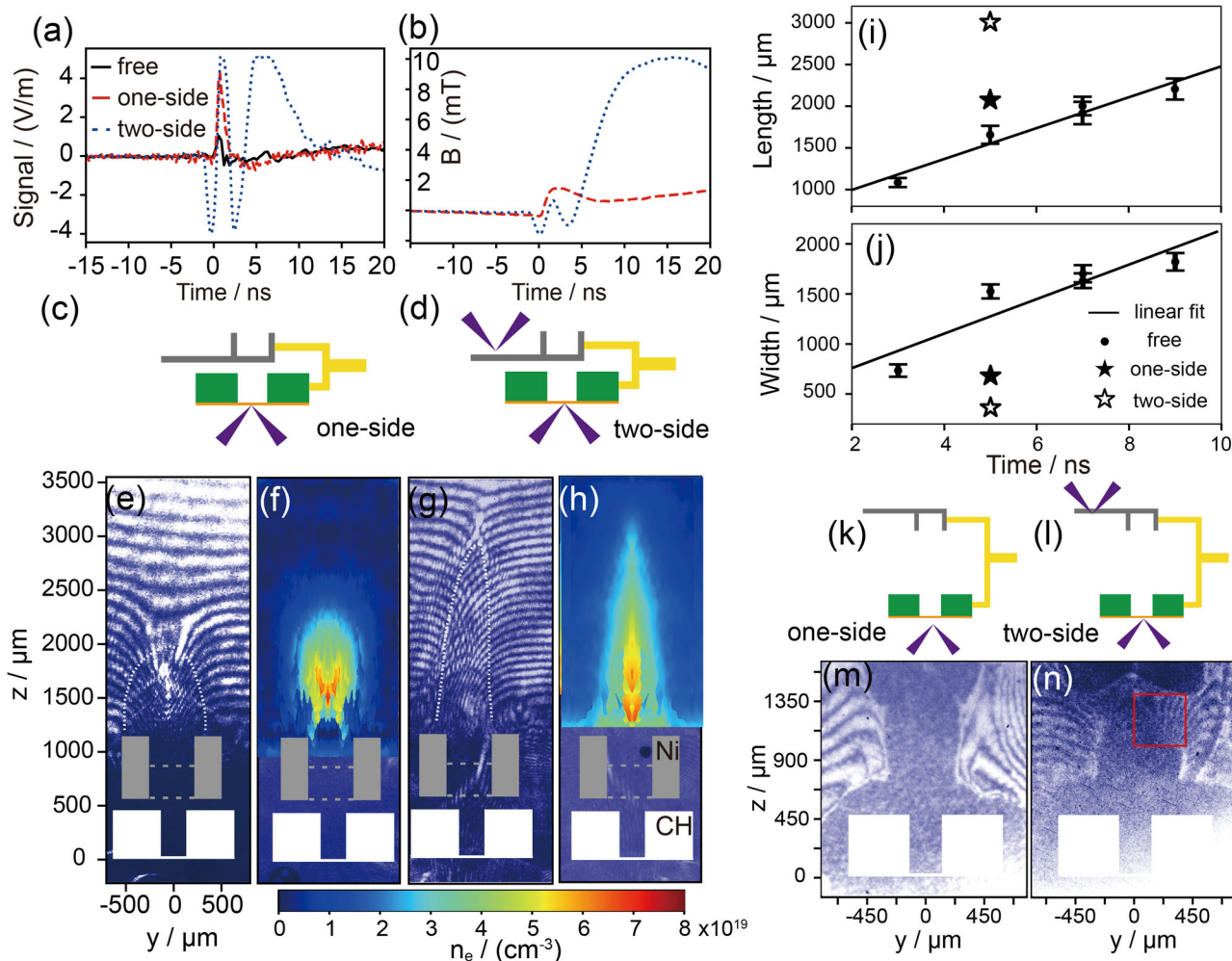


Fig. 4 | Experimental results of laser-driven scaled plasma jets. a, b The B-dot signals and the corresponding integrated magnetic field signal for respectively the free-expansion, one-side, and two-side shots. **c, d** Schematic views of one-side and two-side shots. **e, f** The original Nomarski interference images of plasma outflow densities and the corresponding plasma densities obtained through the inversion program for the one-side shot at $t = T_0 + 5$ ns (where T_0 represents the time at which the driven laser begins to interact with the CH target). **g, h** The corresponding results for the two-sided shot. The colorbar under panel **h** represents the distribution of number density (n_e) in panel **f, h, i, j**. The lengths and widths of the plasma

outflows vary with time during their propagation for all experimental shots, where 'free' represents the free-expansion case of laser-driven plasma outflow. The error bars in panels **i, j** represent the range of uncertainty introduced by different measurement positions when measuring the length and width of the jet in the Nomarski interference images. **k, l** Schematic views of the setup of the one-side and two-side shots for the comparative case [see Fig. 1f]. **m, n** The corresponding Nomarski interference images of plasma outflow densities for the comparative case at $t = T_0 + 5$ ns.

the confinement by toroidal fields, the plasma thermal pressure close to the z -axis (around $y = 0$) is enhanced by twice as large as that in the free-expansion case (comparing the red and green lines), which drives much faster longitudinal expansion of the plasma jet, that is, the jet undergoes acceleration by the enhanced plasma thermal pressure. The plasma streamlines plotted in Fig. 5c also clearly show the jet formation process under the confinement of the toroidal magnetic field, where the isotropic thermal expansion of plasma gradually transforms into a directional transport. Above $z = 1.2$ mm, the maximum number density is close to $1 \times 10^{20} \text{ cm}^{-3}$ [Fig. 5f], and the number density of plasma flow decreases with the distance along the Z -direction, which is similar to the experimental inversion results [see Fig. 4h]. In addition, we also conducted numerical simulations to verify that the mechanical constraints imposed by the Ni posts cannot effectively constrain the lateral expansion of the outflow [see Fig. S9, Fig. S10, and Supplementary Note 5 in the Supplementary].

Figure 5g plots the density map of the CH plasma outflow at a time delay of 5 ns obtained from the simulation for the comparative two-sided case (see the setup of Fig. 4l). The length of outflow is a little shorter than free expansion, and an inverted-triangle-like structure also appears in the experimental results

(see Fig. 4n). The toroidal fields can also confine the plasma outflow to a certain extent, but the position of the maximum Lorentz force is at the top of the outflow, and the direction of the force is downward (see Fig. 5h), which can result in obstructing the outflow propagation in the vertical direction.

Conclusion

In our laboratory experiments, the scaled plasma jet can be regarded as an ideal fluid, where both the viscosity and the thermal diffusivity can be ignored and the plasma is magnetized, because it has the magnetic Reynolds number⁴⁶ of $R_m = Lv/\eta \approx 800$ (η is the plasma resistivity), Reynolds number⁴⁷ of $Re = vL/\nu \approx 5000$ (where ν is the viscosity), and Peclet number⁴⁶ $Pe = vL/\kappa \approx 21$ (where κ is the thermal diffusivity). The detailed calculation process can be referred to the section Supplementary Note 6 in the Supplementary. Therefore, our laboratory-produced jet can be expected scaled up to the YSO jet with the similarity scaling law⁴⁸. Although the strength and topology of magnetic fields in the astrophysical flows still remain a major open question, the estimate for the required magnetic field strength to confine the outflow is roughly comparable to the scaled-up magnetic field strength in our experimental setup (typical mG level in YSO jets).

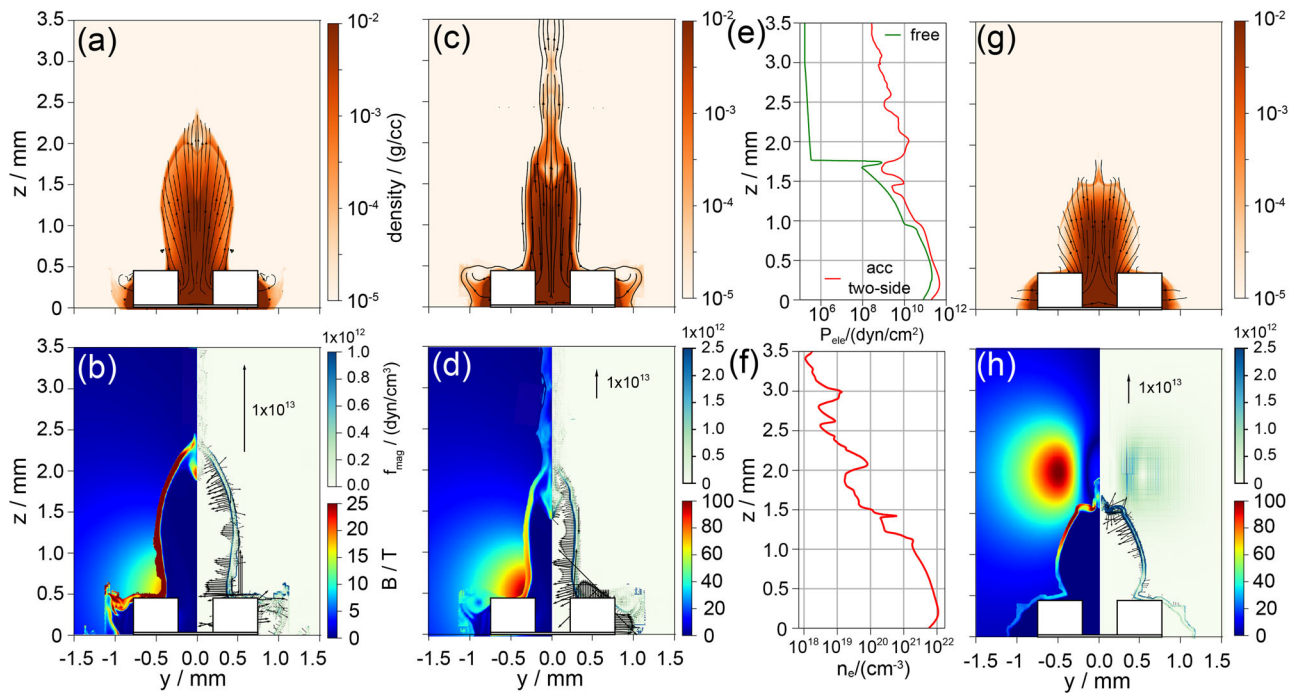


Fig. 5 | 2D magneto-hydrodynamic (RMHD) simulation results for jet collimation and acceleration in the presence of toroidal magnetic fields. **a** Distributions of the plasma density at time $t = T_0 + 5\text{ns}$ (where T_0 represents the time at which the driven laser begins to interact with the CH target.) obtained from the simulations for the one-side case in acceleration scenarios, and panel **b** shows the corresponding distribution of magnetic fields (left part) and Lorentz force (right part), where the black arrow lines represent the force vectors. **c** The corresponding distribution of the plasma density obtained from the simulation for the two-side case in acceleration scenarios at $t = T_0 + 5\text{ns}$, and panel **d** shows the corresponding magnetic fields and

Lorentz force. **e** The plasma thermal pressure along the z -axis ($y = 0$) for, respectively, the two-side case (red line) in acceleration scenarios (panel **c**) and free-expansion case (green line). **f** Profiles along the z -axis of the plasma number density (n_e) at $y = 0$ for in **b**. Panel **g** is the corresponding distribution of the plasma density obtained from the simulation for the comparative two-side case of Fig. 1f. **h** plots the corresponding distribution of magnetic fields and Lorentz force. The color bars on the right side of panels **a**, **c**, and **g** indicate plasma density, while those on the upper half of panels **b**, **d**, and **h** on the right side represent Lorentz forces, and those on the bottom half represent magnetic field strength.

In summary, our scaled laboratory experiments and validated numerical simulations reveal that a narrow YSO jet can be formed from confinement and acceleration of a wide-angle astrophysical plasma outflow in the presence of toroidal magnetic fields. This work not only advances our knowledge of YSO jet formation and collimation dynamics, but also opens up tremendous opportunities in the laboratory to explore jets from a variety of other astrophysical jets, including active galactic nuclei, X-ray binary systems, and pulsar wind nebulae, as well as another toroidal magnetic field relevant astrophysical events, such as the accretion shocks formation⁴⁹, the collision of jets⁵⁰, and so on^{32,51,52}.

Methods

Experiment facility and diagnostics

The all-optical scaled laboratory experiments presented in this work are carried out at the ShenGuang-II (SG-II) laser facility at the National Laboratory on High Power Laser and Physics, Chinese Academy of Sciences. The laser facility can deliver 8 nanosecond-laser pulses. Each pulse has energy of $E_L = 250 \pm 30\text{J}$, a duration of about 1 ns, and a wavelength of 351 nm. The 8 laser pulses are divided into two bunches to irradiate CH and Ni targets respectively, as shown in Fig. 1a, so the total laser energy of every bunch is about 1000 J. The FWHM (full-width at half maximum) of laser spot size, measured by an X-ray pinhole camera, is about 380 μm in diameter, so the corresponding laser intensity for every bunch is about $8.8 \times 10^{14} \text{W/cm}^2$.

The main diagnostics in the experiments are the X-ray pinhole camera, B-dot probe, and optical diagnostics. The X-ray pinhole camera with 20 μm beryllium foil filter is used to monitor the laser spot size and shape when it irradiates on the CH target, whose observation angle is 15° to the horizontal plane. The image for the pinhole camera is given in Fig. S5 in Supplementary Information, and the diameter of the laser spot is about 380 μm as

mentioned above. The strength of the magnetic field is measured by a B-dot probe. The B-dot in our experiment is manufactured by PROLYN Technologies Inc⁵³, and it has high transparency (approx. 86%). The B-dot consists of two differential induction coils, where the electrostatic field pickup created by the plasma can be removed, and the sensor equivalent area $A_{eq} = 2 \times 10^{-1} \text{cm}^2$. The B-dot probe was placed in $(X, Y, Z) = (-44 \text{mm}, 0, 12 \text{mm})$, 46 mm away from the center, and 75° to the vertical plane. For the optical method, the probe laser transversely passes through the interaction region and carries the plasma information, recorded in the CCDs. The spatial distribution of electron density can be given by the Nomarski interferometer, whose details are given in Supplementary Note 2 in Supplementary Information.

The proton radiography experiment is performed in the ShenGuang-II Upgrade (SG-II UP) laser facility at the Chinese Academy of Science. The Multi-MeV proton beam is generated by the interaction between the picosecond laser ($300 \pm 20\text{J}/1\text{ps}$, the corresponding laser intensity is about $5 \times 10^{19} \text{W/cm}^2$) and Au foil through TNSA (Target Normal Sheath Acceleration). The cut-off energy of the high-quality laminar proton beams exceeds 39 MeV, and the deflected protons are finally deposited on the HD-V2 radiochromic film (RCF) stack. The driven ns laser on the open-ended four-post Ni target is about 800 J, whose intensity is similar to the experiment in SG-II. More details about the experimental setup of proton radiography are given in Supplementary (Fig. S7 and Supplementary Note 4).

Radiation hydrodynamic simulation

The 3D and 2D RMHD simulations in this work are carried out by using the code “FLASH”⁴⁵, which has been developed to include many high-energy density physics modeling capabilities⁵⁴ including laser energy deposition, multi-temperature ($T_e \neq T_i \neq T_{rad}$), electron thermal conduction, and radiation transport, etc.

In 2D cylindrical RMHD simulations, the simulation domain size is set as $(r,z) = 3000 \mu\text{m} \times 4000 \mu\text{m}$ with adaptive mesh refinement applied and the highest resolution $2 \mu\text{m}$ achieved. In 3D simulations, the simulation domain size is set as $(x,y,z) = 3000 \mu\text{m} \times 3000 \mu\text{m} \times 4000 \mu\text{m}$ with the highest resolution $10 \mu\text{m}$. The initial conditions including laser and target parameters are all consistent with the experiments. The Courant-Friedrichs-Lewy (CFL) is set as 0.2 and a third-order interpolation is used to reach a balance between accuracy and stability in simulation. The equation of state (EoS) and opacity of solid materials (CH) come from the code BADGER⁵⁵ and IONMIX⁵⁶ respectively, and the initial density of the CH target is set as $\rho_{CH} = 1.05\text{g/cm}^3$. Due to the configuration requirement of the code “FLASH”, a low-density ($1 \times 10^{-7}\text{g/cm}^3$) Helium (He) background plasma is set in the simulations. All the initial temperatures are set to be uniform at room temperature 290 K. The boundary conditions for fluid and radiation transport are all set to open. The toroidal magnetic fields within the simulation are self-consistently implemented from the “Radia” simulation.

Proton radiography simulation

In order to directly compare with the RCF images in the experiment, we perform numerical proton radiography simulation based on the magnetic fields obtained from the “Radia” simulation. We use the “Proton Imaging” unit in Flash code to perform the proton radiography simulation. The simulation setup is the same as the experimental setup. The energy of the injected protons is 30 MeV, and the magnification is also set as $M = 10$.

Path-integrated field reconstruction

The reconstruction of the path-integrated magnetic field Ψ from proton radiography in this work is done by using the program “PROBLEM”⁴³ which uses the Monge-Ampere equation to invert the proton flux information. The basic principle of proton imaging is that the protons are deflected by the Lorentz force arising from the magnetic field generated by an open-ended four-post target, and the lateral deflection velocity can be expressed as

$$\mathbf{v}(\mathbf{x}_{\perp 0}) \approx \frac{e}{m_p c} \hat{\mathbf{z}} \times \int_0^{L_z} \mathbf{B}(\mathbf{x}(s)) ds \quad (1)$$

where e, m_p are the charge and mass of the proton, $\mathbf{x}_{\perp 0}$ is the initial perpendicular position, $\mathbf{x}(s)$ is the proton trajectory. The outgoing protons move in a straight line, then the lateral deflection position \mathbf{x}_{\perp}^s can be amplified as

$$\mathbf{x}_{\perp}^s(\mathbf{x}_{\perp 0}) \approx \frac{h_1 + h_2}{h_1} \mathbf{x}_{\perp 0} + \frac{\mathbf{v}(\mathbf{x}_{\perp 0})}{v_{\text{proton}}} h_2 \quad (2)$$

where v_{proton} is the proton velocity, and $h_1 = 10\text{mm}, h_2 = 90\text{mm}$ are respectively the distance from the proton source to the plasma and the distance from the plasma to the RCF screen and \mathbf{x}_{\perp}^s is the position of the proton on the RCF stack. By the conservation of proton flux on the RCF screen, the flux distribution $\Phi \mathbf{x}_{\perp}^s$ can be expressed as

$$\Phi(\mathbf{x}_{\perp}^s(\mathbf{x}_{\perp 0})) = \sum_{\mathbf{x}_{\perp}^{(s)} = \mathbf{x}_{\perp}^s(\mathbf{x}_{\perp 0})} \frac{\Phi_0}{|\text{Det}(\nabla_{\perp 0}[\mathbf{x}_{\perp}^s(\mathbf{x}_{\perp 0})])|} \quad (3)$$

where Φ_0 is the initial flux distribution, and $\nabla_{\perp 0}$ is the gradient operator with respect to the initial plasma coordinates. Then the path-integrated magnetic field can be obtained by solving the Monge-Ampere⁴⁴ equation (3)

$$\Psi = \int_0^{L_z} \mathbf{B}(\mathbf{x}(s)) ds = -\frac{e}{m_p c} \hat{\mathbf{z}} \times \mathbf{v}(\mathbf{x}_{\perp 0}) \quad (4)$$

In this work, the redistributed proton flux Φ can be obtained from the response function of RCF optical density (OD) to proton dose, which has an almost linear relationship in the low-dose region. The initial proton flux distribution Φ_0 used in the inversion is selective to remove the influence of the four-post target on the initial average flux of protons.

Data availability

All data that support the findings of this study are available from the corresponding author upon reasonable request.

Code availability

The FLASH code is available for download from <https://flash.rochester.edu/site/flashcode>. PROBLEM solver is an open code of the proton radiography reconstruction algorithm of Bott (2017), the source code is available for download from <https://github.com/flashcenter/PROBLEM>. The Radia code can be downloaded from <http://www.esrf.eu/Accelerators/Groups/InsertionDevices/Software/Radia>.

Received: 14 June 2023; Accepted: 11 March 2024;

Published online: 23 March 2024

References

1. Fulai, G. & Mathews, W. G. Cosmic-ray-dominated AGN Jets and the Formation of X-ray Cavities in Galaxy Clusters. *Astrophys. J.* **728**, 121 (2011).
2. Stefano, A. et al. The blazar TXS 0506+ 056 associated with a high-energy neutrino: insights into extragalactic jets and cosmic-ray acceleration. *Astrophys. J. Lett.* **863**, L10 (2018).
3. Shu, F. H., Najita, J., Ostriker, E. C. & Shang, H. Magnetocentrifugally driven flows from young stars and disks. V. Asymptotic collimation into jets. *Astrophys. J.* **455**, L155 (1995).
4. Bally, J. Protostellar outflows. *Annu. Rev. Astron. Astrophys.* **54**, 491–528 (2016).
5. Lee, C.-F. et al. Unveiling a magnetized jet from a low-mass protostar. *Nat. Commun.* **9**, 4636 (2018).
6. Dawei, Y. et al. Laboratory investigation of astrophysical collimated jets with intense lasers. *Astrophys. J.* **860**, 146 (2018).
7. Burrows, C. J. et al. Hubble Space Telescope Observations of the Disk and Jet of HH 30. *ApJ* **473**, 437–451 (1996).
8. Frank, A. et al. Effects of cooling on the propagation of magnetized jets. *Astrophys. J.* **494**, L79 (1998).
9. Matt, S., Winglee, R. & Bohm, K.-H. Collimation of a central wind by a disc-associated magnetic field. *Monthly Not. R. Astronom. Soc.* **345**, 660–670 (2003).
10. Kato, Y., Mineshige, S. & Shibata, K. Magnetohydrodynamical accretion flows: formation of magnetic tower jet and subsequent quasi-steady state. *Prog. Theor. Phys. Suppl.* **155**, 353–354 (2004).
11. Chrysostomou, A., Lucas, P. W. & Hough, J. H. Circular polarimetry reveals helical magnetic fields in the young stellar object HH 135-136. *Nature* **450**, 71–73 (2007).
12. Carrasco-Gonzalez, C. et al. A magnetized jet from a massive protostar. *Science* **330**, 1209–1212 (2010).
13. Reipurth, B. & Bally, J. Herbig-haro flows: probes of early stellar evolution. *Annu. Rev. Astron. Astrophys.* **39**, 403–455 (2001).
14. Warren-Smith, R. F. & Scarrott, S. M. Polarimetry and magnetic field structure of the Herbig-Haro objects HH1 and HH2 and their environment. *Monthly Not. R. Astronom. Soc.* **305**, 875–897 (1999).
15. Kwon, J. et al. Magnetic field structure of the HH 1-2 region: near-infrared polarimetry of point-like sources. *Astrophys. J.* **708**, 758–769 (2010).
16. Frank, A. et al. Jets and outflows from star to cloud: observations confront theory. in *Protostars Planets VI*. <https://doi.org/10.48550/arXiv.1402.3553> (2014).
17. Soker, N. The jet feedback mechanism (JFM) in stars, galaxies and clusters. *N. Astron. Rev.* **75**, 1–23 (2016).

18. Krumholz, M. R. & Federrath, C. The role of magnetic fields in setting the star formation rate and the initial mass function. *Front. Astron. Space Sci.* **6**, 7 (2019).
19. Blandford, R. D. & Payne, D. G. Hydromagnetic flows from accretion discs and the production of radio jets. *Monthly Not. R. Astronom. Soc.* **199**, 883–903 (1982).
20. Spruit, H. C. in *Evolutionary Processes in Binary Stars* (eds. Wijers, R.A.M.J., Davies, M.B., Tout, C.A.) p. 249 (Cambridge University Press, Cambridge, 1996).
21. Ray, T. P. & Ferreira, J. Jets from young stars. *N. Astron. Rev.* **93**, 101615 (2021).
22. Shang, H., Krasnopolsky, R. & Liu, C. F. A unified model for bipolar outflows from young stars: apparent magnetic jet acceleration. *Astrophys. J. Lett.* **945**, L1 (2023).
23. Ciardi, A. et al. Astrophysics of magnetically collimated jets generated from laser-produced plasmas. *Phys. Rev. Lett.* **110**, 025002 (2013).
24. Albertazzi, B. et al. Laboratory formation of a scaled protostellar jet by coaligned poloidal magnetic field. *Science* **346**, 325–328 (2014).
25. Revet, G. et al. Laboratory disruption of scaled astrophysical outflows by a misaligned magnetic field. *Nat. Commun.* **12**, 762 (2021).
26. Lei, Z. et al. Numerical study of the knot structure in scaled protostellar jets by laboratory laser-driven plasmas. *Plasma Phys. Control. Fusion* **62**, 095020 (2020).
27. Hsu, S. C. & Bellan, P. M. Experimental identification of the kink instability as a poloidal flux amplification mechanism for coaxial gun spheromak formation. *Phys. Rev. Lett.* **90**, 215002 (2003).
28. Suzuki-Vidal, F. et al. Generation of episodic magnetically driven plasma jets in a radial foil Z-pinch. *Phys. Plasmas* **17**, 112708 (2010).
29. Begelman, M. C. Instability of toroidal magnetic field in jets and plerions. *Astrophys. J.* **493**, 291–300 (1998).
30. Giannios, D. & Spruit, H. C. The role of kink instability in Poynting-flux dominated jets. *Astronom. Astrophys.* **450**, 887–898 (2006).
31. Alves, E. P., Zrake, J. & Fiuzza, F. Efficient nonthermal particle acceleration by the kink instability in relativistic jets. *Phys. Rev. Lett.* **121**, 245101 (2018).
32. Lebedev, S. V., Frank, A. & Ryutov, D. D. Exploring astrophysics-relevant magnetohydrodynamics with pulsed-power laboratory facilities. *Rev. Mod. Phys.* **91**, 025002 (2019).
33. Moody, J. D. et al. Increased ion temperature and neutron yield observed in magnetized indirectly driven D2-filled capsule implosions on the national ignition facility. *Phys. Rev. Lett.* **129**, 195002 (2022).
34. Bhuvana, S. & Tang, X.-Z. The mitigating effect of magnetic fields on Rayleigh-Taylor unstable inertial confinement fusion plasmas. *Phys. Plasmas* **20**, 056307 (2013).
35. Walsh, C. et al. Application of Non-Uniform Magnetic Fields to Inertial Confinement Fusion Implosions. In *APS Division of Plasma Physics Meeting Abstracts*. **2023**, JO07-014 (2023).
36. Shigemori, K. et al. Experiments on radiative collapse in laser-produced plasmas relevant to astrophysical jets. *Phys. Rev. E* **62**, 8838–8841 (2000).
37. Yurchak, R. et al. Experimental demonstration of an inertial collimation mechanism in nested outflows. *Phys. Rev. Lett.* **112**, 155001 (2014).
38. Loupias, B. et al. Supersonic-jet experiments using a high-energy laser. *Phys. Rev. Lett.* **99**, 265001 (2007).
39. Will, F. et al. Filamentation instability of counterstreaming laser-driven plasmas. *Phys. Rev. Lett.* **111**, 225002 (2013).
40. Zhu, B. J. et al. Strong magnetic fields generated with a simple open-ended coil irradiated by high power laser pulses. *Appl. Phys. Lett.* **107**, 261903 (2015).
41. See <http://www.esrf.eu/Accelerators/Groups/InsertionDevices/Software/Radia> for information about the code Radia.
42. Zhao, Z. H. et al. Laboratory observation of plasmoid-dominated magnetic reconnection in hybrid collisional-collisionless regime. *Commun. Phys.* **5**, 247 (2022).
43. Bott, A. et al. Proton imaging of stochastic magnetic fields. *J. Plasma Phys.* **83** 905830614 (2017).
44. Kugland, N. L. et al. Invited article: relation between electric and magnetic field structures and their proton-beam images. *Rev. Sci. Instrum.* **83**, 101301 (2012).
45. Fryxell, B. et al. FLASH: an adaptive mesh hydrodynamics code for modeling astrophysical thermonuclear flashes. *Astrophys. J. Suppl. Ser.* **131**, 273–334 (2000).
46. Brandenburg, A. & Subramanian, K. Astrophysical magnetic fields and nonlinear dynamo theory. *Phys. Rep.* **417**, 1–209 (2004).
47. Drake, R. P. *High-Energy-density Physics: Foundation of Inertial Fusion and Experimental Astrophysics* (2nd edition). (Springer, 2018).
48. Ryutov, D. D. et al. Magnetohydrodynamic scaling: From astrophysics to the laboratory. *Phys. Plasmas* **8**, 1804–1816 (2001).
49. Revet, G. et al. Laboratory unraveling of matter accretion in young stars. *Sci. Adv.* **3**, e1700982 (2017).
50. Li, C. K. et al. Structure and dynamics of colliding plasma jets. *Phys. Rev. Lett.* **111**, 235003 (2013).
51. Remington, B. A. Modeling astrophysical phenomena in the laboratory with intense lasers. *Science* **284**, 1488–1493 (1999).
52. Remington, B. A., Drake, R. P. & Ryutov, D. D. Experimental astrophysics with high power lasers and Z pinches. *Rev. Mod. Phys.* **78**, 755–807 (2006).
53. See <https://www.prodyntech.com/wp-content/uploads/2013/10/pan606.pdf> for information about the B-dot probe.
54. Tzeferacos, P. et al. FLASH MHD simulations of experiments that study shock-generated magnetic fields. *High. Energy Density Phys.* **17**, 24–31 (2015).
55. Heltemes, T. A. & Moses, G. A. BADGER v1.0: a Fortran equation of state library. *Comput. Phys. Commun.* **183**, 2629–2646 (2012).
56. Macfarlane, J. J. IONMIX-A code for computing the equation of state and radiative properties of LTE and non-LTE plasmas. *Comput. Phys. Commun.* **56**, 259–278 (1989).

Acknowledgements

This work is supported by the National Key R&D Program of China, grants No. 2022YFA1603200, No. 2022YFA1603201, and No.2022YFA1603204; National Natural Science Foundation of China, grants No.11825502, No. 11921006, No. 12135001 and Strategic Priority Research Program of CAS, Grant No. XDA25050900. B.Q. acknowledges support from the National Natural Science Funds for Distinguished Young Scholars, grant No. 11825502. Z.L. is supported by the China Postdoctoral Science Foundation, No. 2023M730334. The simulations are carried out on the Tianhe-2 supercomputer at the National Supercomputer Center in Guangzhou. The software used in this work was developed in part by the DOE NNSA and DOE Office of Science-supported Flash Center for Computational Science at the University of Chicago and the University of Rochester.

Author contributions

B.Q. proposed and was in charge of the research campaign as the principal investigator. Z.L., Z.H.Z., W.S., D.W.Y., Y.X., W.Q.Y., S.K.H., L.C. performed the experiments, with support from Z.Z., J.Y.Z., W.W., B.Q.Z., W.M.Z., C.T.Z., S.P.Z., J.Q.Z. and X.T.H. H.H.A. performed the proton radiography experiments and Z.L., Z.H.Z. and B.Q. analyzed the data. Z.L. and Z.H.Z. performed and analyzed the FLASH simulations, as well as the Radia code. Z.L. and L.X.L. developed the model of toroidal field generation and analyzed the proton radiography data. Z.L. and B.Q. wrote the bulk of the paper. All authors contributed to the discussions and approved the final version of the manuscript.

Competing interests

The authors declare no competing interests.

Additional information

Supplementary information The online version contains supplementary material available at <https://doi.org/10.1038/s42005-024-01594-w>.

Correspondence and requests for materials should be addressed to B. Qiao.

Peer review information *Communications Physics* thanks the anonymous reviewers for their contribution to the peer review of this work. A peer review file is available.

Reprints and permissions information is available at <http://www.nature.com/reprints>

Publisher's note Springer Nature remains neutral with regard to jurisdictional claims in published maps and institutional affiliations.

Open Access This article is licensed under a Creative Commons Attribution 4.0 International License, which permits use, sharing, adaptation, distribution and reproduction in any medium or format, as long as you give appropriate credit to the original author(s) and the source, provide a link to the Creative Commons licence, and indicate if changes were made. The images or other third party material in this article are included in the article's Creative Commons licence, unless indicated otherwise in a credit line to the material. If material is not included in the article's Creative Commons licence and your intended use is not permitted by statutory regulation or exceeds the permitted use, you will need to obtain permission directly from the copyright holder. To view a copy of this licence, visit <http://creativecommons.org/licenses/by/4.0/>.

© The Author(s) 2024